Nuclear Materials and Energy 26 (2021) 100890

Contents lists available at ScienceDirect

Nuclear Materials and Energy

journal homepage: www.elsevier.com/locate/nme

Broadening of the power fall-off length in a high density, high confinement H-mode regime in ASDEX Upgrade

M. Faitsch [a,*], T. Eich [a], G.F. Harrer [b], E. Wolfrum [a], D. Brida [a], P. David [a], M. Griener [a], U. Stroth [a,c], The ASDEX Upgrade Team [1], The EUROfusion MST1 Team [2]

[a] Max-Planck-Institute for Plasma Physics, Boltzmannstr. 2, 85748 Garching, Germany
[b] Institute of Applied Physics, TU Wien, Fusion@ÖAW, Wiedner Hauptstr. 8-10, 1040 Vienna, Austria
[c] Physik Department E28, Technische Universität München, 85748 Garching, Germany

ARTICLE INFO

Keywords:
Power exhaust
Scrape-off layer
Infrared thermography

ABSTRACT

The search for scenarios in which tolerable power exhaust is combined with good confinement must involve high separatrix densities. We present here the first infrared thermography measurements at ASDEX Upgrade in a high density, high confinement H-mode regime in which no type-I ELMs are present. This regime was formerly called type-II ELM or small ELM regime to distinguish it from type-I ELMs. We report on a broadening of the power fall-off length in this regime of up to a factor of four compared to low density inter type-I ELM conditions. This broadening is correlated to an increased filament detection rate as well as an increase in the pressure close to the separatrix. The broadening of the fall-off length decreases the peak heat flux, while the filaments lead to a quasi-continuous transport into the scrape-off layer and onto the divertor.

1. Introduction

Power exhaust is one of the key challenges on the route towards a tokamak fusion reactor. The leading parameter to estimate the steady state power load onto the divertor target is the width of the power carrying layer outside the separatrix. The power carrying width is characterised by an exponential fall-off length λ_q in the scrape-off layer, commonly inferred from infrared (IR) thermography measurements at the divertor target [1]. An empirical ITPA-multi-machine approach revealed the poloidal magnetic field at the outer mid-plane as leading parameter setting λ_q in H-mode [2]. One of the remarkable outcomes was the absence of a machine size dependence, leading to a decrease of the predicted λ_q towards larger machines like ITER due to their larger magnetic fields.

A heuristic model based on (neo)-classical drifts is able to explain the dependence on the poloidal magnetic field as well as the independence of the machine size [3]. Recent gyro-kinetic simulations with the XGC1 code using ITER parameters found a widening of λ_q due to electron turbulence dominating at high poloidal magnetic field and large machine size [4].

The ITPA-multi-machine approach describes the power fall-off length in H-mode between type-I edge localised modes (ELMs). These type-I ELMs lead to transient power loads that are expected to reduce the life time of the first wall. This is why they need to be mitigated in ITER [5] and have to be avoided completely for reactor-sized devices [6]. Active tools to mitigate or suppress type-I ELMs as well as alternative regimes are studied on many present-day machines.

A regime at high density in which no type-I ELMs are present exists on ASDEX Upgrade at high triangularity, close-to-double-null [7,8]. It combines a high plasma core performance ($H_{98,y2} \simeq 0.9$–1.0, $n_{e,core} \simeq 0.9\, n_{GW}$) with a high separatrix density ($n_{e,sep} \simeq 0.4\, n_{GW}$), close to a previously reported limit [9,10]. High separatrix density is a key parameter in order to reach high radiative power losses and divertor detachment [11,12]. In previous studies this regime was referred to as small ELMs [13,14] or type-II ELMs [7,8,15,16] to distinguish them from type-I ELMs. We will use the term small ELMs to refer to previous studies, but will otherwise not classify the phenomenon with the term *ELM* due to the connotation with an MHD event affecting the complete pedestal gradient region. We choose to call the regime quasi-continuous exhaust (QCE) due to enhanced filamentary transport at the plasma edge compared to inter type-I ELM phases. These filaments are linked to a normalised pressure gradient close to the critical value of ideal ballooning modes at the pedestal bottom [13] and also with a turbulence control parameter [17]. Both are increased in the QCE regime

* Corresponding author.
E-mail address: Michael.Faitsch@ipp.mpg.de (M. Faitsch).
[1] See author list of "MEYER, H. et al., Nucl. Fusion **59** (2019) 112014".
[2] See author list of "LABIT, B. et al., Nucl. Fusion **59** (2019) 086020".

https://doi.org/10.1016/j.nme.2020.100890
Received 30 July 2020; Received in revised form 18 November 2020; Accepted 14 December 2020
Available online 18 December 2020

since the separatrix density is increased leading to a higher pressure and collisionality.

High separatrix density operation typically hampers IR thermography measurements. On the one hand detachment processes modify the direct link between divertor target profiles and scrape-off layer quantities. On the other hand the ITER similar tungsten divertor in ASDEX Upgrade with a vertical target poses diagnostics limitations. In order to observe the vertical target with a high spatial resolution a toroidal viewing geometry is chosen, increasing the path inside the cold plasma region close to the X-point and along the divertor leg which increases the disturbing impact of volume radiation such as bremsstrahlung. The low emissivity of tungsten reduces the photon emission compared to e.g. carbon, increasing the influence of the volume radiation.

In order to investigate the power fall-off length in the QCE regime we report here on dedicated experiments using main chamber fuelling and attached divertor conditions together with an increased safety factor in order to reduce the amount of gas puff. This allowed for the first time scrape-off layer power fall-off length estimations from IR thermography in this regime.

The paper is organised as follows: Section 2 introduces the experimental setup and presents first scrape-off layer power fall-off length measurements by infrared thermography showing a broadening of the power fall-off length in the QCE regime compared to inter type-I ELM phases. The power fall-off length is compared to published scaling law predictions in Section 3. Section 4 discusses the parallel and perpendicular heat transport in the QCE regime and a link to an increase of filament frequency and the scrape-off layer kinetic parameters in the vicinity of the separatrix. A discussion and conclusions are provided in Section 5.

2. Experimental setup

The ASDEX Upgrade discharge # 36165 was designed to allow IR measurements at the outer target in a regime with increased filamentary transport. Because these filaments appear at high separatrix density and at high shaping, and because they can occur together with type-I ELMs, the plasma is shaped early in the discharge with an upper triangularity $\delta_{up} = 0.27$ from 2.0 s on. The density is increased stepwise by gas puffing in the main chamber in an effort to minimise bremsstrahlung in the field of view of the IR camera. The filaments become increasingly frequent, first in between type-I ELMs, but from 5.0 s on no type-I ELMs are present anymore.

Fig. 1 shows time traces of ASDEX Upgrade discharge # 36165. After the initial plasma ramp-up, the discharge is stable from around 2.0 s up to 6.8 s when the gas puff and heating power is ramped down. The discharge is in a diverted lower single null configuration with stable strike line position from around 1.8 s on which is needed to infer reliable data from the IR system. The plasma current is $I_p = 0.8$ MA and the toroidal magnetic field on the axis is $B_{tor} = -2.5$ T leading to an edge safety factor of $q_{95} = 5.3$. Constant additional heating power of $P_{NBI} = 5.0$ MW from neutral beam injection (NBI) and $P_{ECRH} = 2.75$ MW from central electron cyclotron resonance heating (ECRH) is applied. The plasma radiation increases from $P_{rad} = 3.0$ MW to 4.0 MW due to the step-wise increase of deuterium fuelling from the main chamber. While a constant divertor fuelling of $D_{div} = 5.0 \cdot 10^{21} \frac{el}{s}$ is applied, the main chamber gas flux is increased in steps of $D_{main} = 5.0 \cdot 10^{21} \frac{el}{s}$ up to a level of $20 \cdot 10^{21} \frac{el}{s}$. The core and edge densities taken from the DCN laser interferometer [18] increase during the discharge. The scrape-off layer currents measured at the outer target by shunts is shown as an ELM monitor. The ELM amplitude decreases from 4.0 s to 5.0 s and type-I ELMs vanish completely afterwards. The divertor electron temperature T_{div} inferred from these scrape-off layer currents [19] is chosen as an indication for attached plasma conditions. For a partially detached divertor T_{div} drops below 10 eV [20] while it stays above 30 eV in this discharge. The temperature inferred from the scrape-off layer currents might be overestimated in a highly shaped plasma because part of the current reaches the upper divertor, not considered for the estimate of T_{div}. Langmuir probe (LP) measurements indicate the target electron temperature being around 15–20 eV. However, no LP data is available at the location of the maximum heat flux making this a lower limit of the peak temperature. From both estimates it is concluded that the discharge is in an attached, high recycling divertor regime.

We report in detail on the divertor target power load profiles in order to measure the scrape-off layer power fall-off length. The power load is inferred from high resolution infrared thermography (IR) data [21] using an implicit version [22] of the THEODOR code [23]. Fig. 2 shows divertor heat flux profiles at three different levels of main chamber deuterium gas fuelling. At the lowest fuelling level the profile is taken between type-I ELMs at 2.05 s. During type-I ELMs non thermal radiation causes exaggerated background heat flux leading to a negative background in the inter-ELM phases in order to fulfil the energy conservation within THEODOR, see e.g. [24]. This negative heat flux is in the order of $1 \frac{MW}{m^2}$ and subtracted for the profile analysis. At medium and high fuelling levels no type-I ELMs are present and the profile is averaged over filaments reaching the divertor at 5.05 s and 6.05 s, respectively. The IR frame rate was 1.5 kHz and the averaging is performed over 10 profiles (6.6 ms) for all three profiles. The comparison of these heat flux profiles leaves out the impact of type-I ELMs, which broaden the energy deposition but are extrapolated to violate the transient damage limit in ITER. Therefore, the profiles of medium and high fuelling rate contain the total energy during the given plasma period, as no type-I ELMs are cut out, and yet the peak is reduced because of the broadening. The inter ELM profile at low fuelling level is in line with the ITPA-multi-machine scaling law [2]

$$\lambda_q = 0.63 \cdot B_{pol,OMP}. \quad (1)$$

With increasing fuelling the power fall-off length increases significantly, up to a factor four within this discharge. As described in Section 4 and [25] this increase in filamentary transport comes along with both, an increase in filament frequency and radial propagation velocity.

One concern about a broad scrape-off layer and filamentary transport are power loads onto the first wall outside the divertor region. This can be estimated by a power balance. The loss channels that we take into account are radiative power losses from bolometric reconstructions [26], divided into main chamber and divertor radiation, and power flux onto the divertor from IR thermography observing the lower outer divertor and the complete upper divertor.[3] The power load onto the lower inner divertor is not captured by IR thermography. However, this contribution is assumed to be small due to the high density leading to a detachment of the inner divertor in typical ASDEX Upgrade discharges.

Fig. 3 shows the power balance for # 36165. All contributions are normalised to the net input power, accounting for changes in stored energy, NBI charge exchange losses as well as NBI losses in the scrape-off layer. The data is ELM averaged by a mean filter of 0.2 s. It can be seen that the main chamber radiation increases only slightly. This is in line with an increasing fuelling and a low effective charge in the confined plasma region. Impurity accumulation is not observed. Such conditions are commonly observed in the QCE regime showing that the absence of impurity outflow by type-I ELMs is compensated by filamentary transport. The radiation in the lower divertor volume increases with increasing fuelling. Simultaneously, the power reaching the lower outer divertor decreases. The power reaching the upper divertor increases, especially after the transition to the type-I ELM free phase after 5 s. Since the upper divertor is not connected to the main plasma the enhanced power load is a sign of increased cross-field transport leading to a widening of λ_q. The radial distance between the separatrices from the upper and lower X-points mapped to the

[3] For viewing geometry see Fig. 1 of [27].

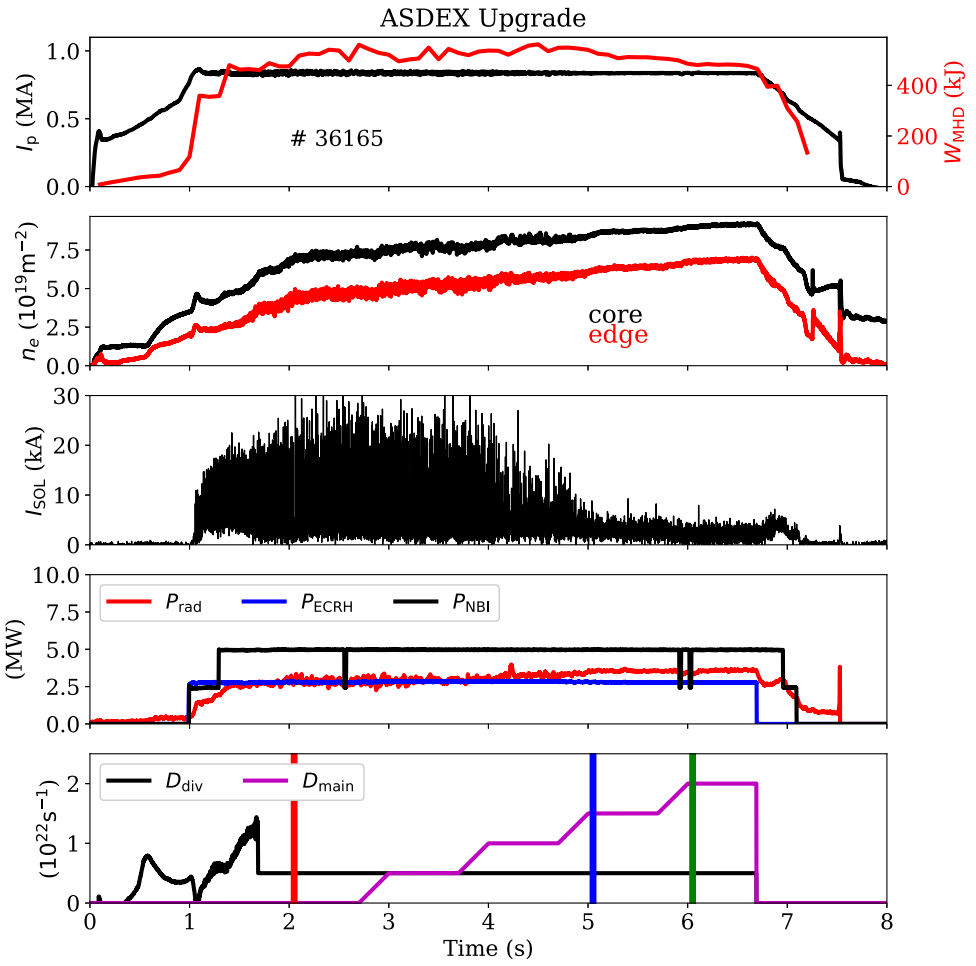

Fig. 1. Time traces of ASDEX Upgrade discharge #36165. The first panel shows plasma current I_p (black) and stored energy W_{MHD} (red). The second panel shows core (black) and edge (red) density measured with the DCN interferometer. The scrape-off layer current measured at the outer divertor target represents an ELM monitor and is shown in the third panel. Heating power from NBI (black) and ECRH (blue) together with the total radiated power P_{rad} are shown in the fourth panel. The lowest panel shows the gas fuelling from divertor (black) and main chamber (magenta) gas valves. Marked are in colour the time points used for the three profiles in Fig. 2 (right).

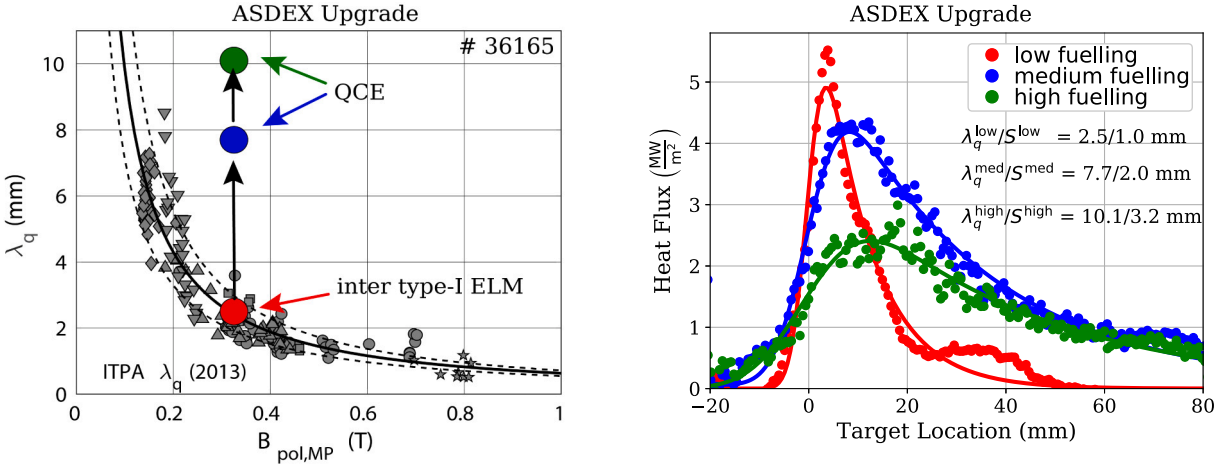

Fig. 2. (left) Measured power fall-off lengths λ_q for low (red), medium (blue) and high (green) fuelling are compared to data from the ITPA-multi-machine data base (grey) which was obtained in inter-ELM phases. (right) Measured heat flux profiles, with the low fuelling case being inter-type-I ELM, whereas in the medium and high fuelling phases no type-I ELMs were present. The values for the measured λ_q and divertor broadening S is extracted from the fit with a flux expansion $f_x = 3.9$ from the magnetic reconstruction. For the low fuelling inter-ELM profile a negative background heat flux of $1.3\,\frac{MW}{m^2}$ is subtracted. The profiles are taken at 2.05 s, 5.05 s and 6.05 s, also marked in Fig. 1 lowest panel.

outer mid-plane (OMP) is 19 mm. The increase of λ_q from around 2.5 mm to 10 mm causes an increased fraction of the power reaching the upper divertor in the QCE phases as well as during type-I ELMs. The power balance accounts for about 80% of the input power. In ASDEX Upgrade discharges with high impurity seeding and detached divertor, the radiated power accounts for up to 90% of the net input power [28].

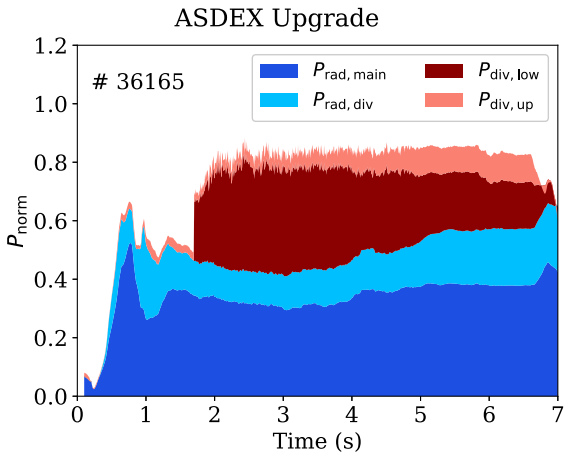

Fig. 3. Power balance for # 36165. The power is normalised to the net input power. The radiated power is divided into main chamber radiation above the lower X-point ($P_{rad,main}$) and divertor power below the lower X-point ($P_{rad,div}$) from bolometric reconstruction. The divertor power is calculated with IR thermography for the lower outer divertor target ($P_{div,low}$) and the complete upper divertor ($P_{div,up}$). The lower inner divertor is not monitored in the given plasma shape.

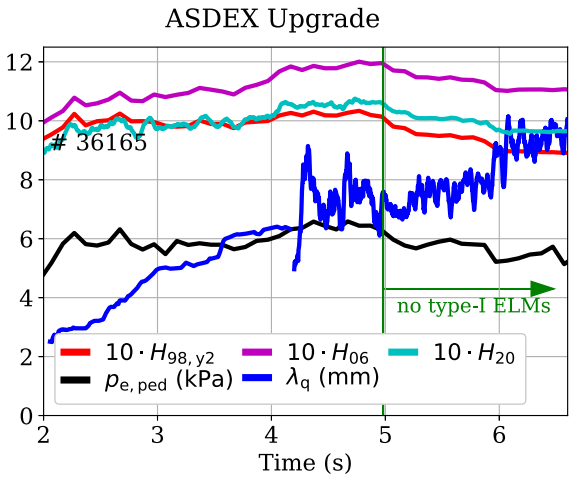

Fig. 4. Temporal evolution of power fall-off length λ_q (blue), pedestal top pressure (black) and three different energy confinement factors: $H_{98,y2}$ (red) [34], H_{06} (magenta) [36] and H_{20} (light blue) [37].

Here we focus on relative changes, showing a constant output power combining radiation and IR measured power onto the lower outer and the upper divertor. We conclude from this that no significant filament related heat flux to the first wall is present in this discharge, despite the widening of λ_q. However, there are indications from temperature measurements of components of the thermal helium beam (THB) diagnostics [29] that an increased power load is present in remote areas at the low field side mid-plane. The absolute magnitude of the first wall power load needs further investigations, but it is small compared to the power reaching the divertor targets.

3. Comparison of measured scrape-off layer broadening with scaling law predictions

Recent studies have shown that the power fall-off length is anti-correlated to confinement in L-mode, I-mode and in between type-I edge localised modes (ELMs) in H-mode [30–33]. In this context it is noteworthy that the poloidal magnetic field B_{pol} dependence of the λ_q scaling Eq. (1) is inverse to that of the energy confinement scaling for ITER [34]

$$\tau_E \propto B_{pol} P^{-0.7} \tag{2}$$

with P being the heating power. Fig. 4 shows in black the temporal evolution of the pressure taken at $\rho_{pol} = 0.95$ from the integrated data analysis (IDA) framework [35] as representation of the pedestal top electron pressure $p_{e,ped}$. It can be seen that $p_{e,ped}$ does not vary significantly, although it decreases slightly after 5.0 s, the time point after which type-I ELMs are no longer present. Additionally, the energy confinement time normalised to three different H-mode confinement scalings is shown, expressed in the H-factors $H_{98,y2}$ [34] (red), H_{06} [36] (magenta) and H_{20} [37] (cyan). Although it was shown in [38] that $H_{98,y2}$ is inappropriate for very high Greenwald fractions [39] of $n_{GW} > 0.8$, it is commonly used. The main difference between the scaling laws is a reduced exponent in the density dependence of the two newer scaling laws compared to $H_{98,y2}$. All three energy confinement factors start with a value of around 1.0 in this discharge. Due to the rising density the scaling factors deviate in the later phase, however, showing a very similar trend. After 5.0 s all exhibit a drop of around 10% when transitioning to the phase without type-I ELMs. It has to be noted that this discharge has a high core collisionality whereas we expect higher temperatures and therefore low core collisionality in a larger machine and, thus, extrapolations of the confinement time have to be taken with great care. The power fall-off length increases continuously as shown in blue. Only inter-ELM λ_q values are used between 2.0 s and 4.2 s and a moving mean filter with 30 time points is applied. ELMs are too frequent to reliably filter them after 4.2 s in the IR data and no type-I ELMs are present after 5.0 s. The increased fluctuation in the measured λ_q value in the time window between 4.2 s and 5.0 s is attributed to the presence of ELMs leading to a larger variation in divertor target power load. A moving mean filter with 50 time points (33 ms) is applied for data after 4.2 s. The increase of the power fall-off length is gradual and does not set in after the type-I ELMs vanish. The gradual increase is in line with previous studies showing that small ELMs can co-exist with type-I ELMs and finally suppress type-I ELMs as they cause sufficient transport to tailor the pedestal shape in a way that the peeling-ballooning stability boundary is not reached [13].

For the power fall-off length various scaling expressions were published in recent years. However, most of them are from measurements in plasma discharges with low separatrix density, i.e. either in inter type-I ELM H-mode conditions or a combination of multiple confinement regimes. Fig. 5 shows the measured λ_q together with selected scaling law predictions which are for ASDEX Upgrade and JET ([1], *Eich2011* in cyan) and the ITPA-multi-machine data base (Eq. (1), *ITPA2013* in red). Both scaling laws use global plasma parameters which are constant in this discharge. They are able to describe the low gas puff, inter type-I ELM λ_q value taken at around 2.0 s. The increase of λ_q is not recovered. Additionally, two scaling laws using the volume averaged pressure [30] (*Brunner2018* in yellow) and the pedestal pressure [32] (*Silvagni2020* in black) are shown. As shown in Fig. 4 the pedestal pressure is not changing significantly in this discharge. Therefore also the scaling laws predict constant values throughout the discharge, which are below the measured λ_q values already in the low fuelling phase.

A recent extension of the ITPA-multi-machine scaling law obtained from Thomson scattering (TS, [40]) measurements yields [17]

$$\lambda_q \propto \frac{1}{B_{pol}} \cdot \left(1 + 2.1\alpha_t^{1.7}\right) \tag{3}$$

It scales with B_{pol} similar to Eq. (1) but has an additional term with a turbulence parameter α_t, defined in Eq. 12 of [17]

$$\alpha_t = 3 \cdot 10^{-18} q_{cyl} R_{geo} \frac{n_{e,sep}}{{T_{e,sep}}^2} Z_{eff}. \tag{4}$$

With the relation $\lambda_q = \frac{2}{7}\lambda_{T_e}$ from Spitzer–Härm electron heat conduction which was shown to match in ASDEX Upgrade for regimes

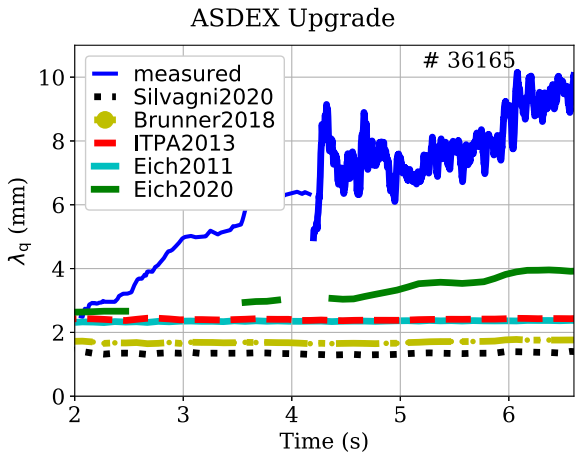

Fig. 5. Temporal evolution of power fall-off length λ_q (blue) and scaling law predictions: Silvagni2020 (black) [32], Brunner2018 (yellow) [30], ITPA2013 (red) [2], Eich2011 (cyan) [1] and Eich2020 (green) [17].

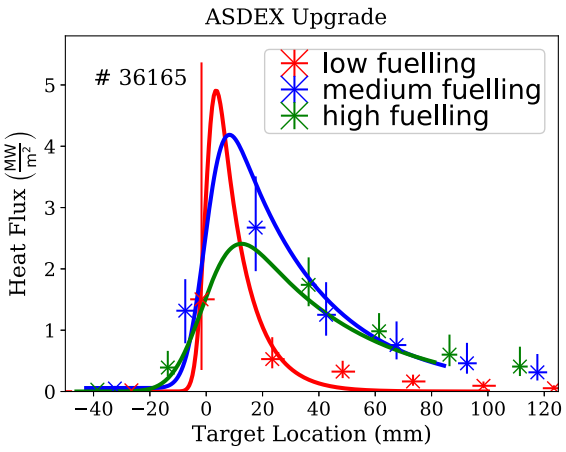

Fig. 6. Heat flux profiles from LP averaged for 400 ms with type-I ELMs being removed. The large error-bar in the red data point around 0 mm originates in the probe being very close to the strike line position leading to a large variation of impinging heat flux with small variations in the strike line position. The probe closest to the strike line in the high fuelling time interval (green) is saturated during filaments and is excluded. The solid lines represent the heat flux profiles from IR.

in which both measurements are available [27,32,41]. The electron temperature fall-off length is calculated using an exponential fit to the TS data around the separatrix including the profile just inside the separatrix as described in [17]. Scaling law Eq. (3) (*Eich2020* in green) predicts a broadening of λ_q in this discharge. However, the magnitude of the broadening is significantly lower than the measured one. The broadening can be attributed to α_t which is used as a measure of the turbulence level around the separatrix [17]. Generally, an increase of α_t is correlated to a reduction in $H_{98,y2}$ [17], which can also be observed in the presented discharge.

A recent numerical study with the gyro-kinetic XGC1 code predicts for ITER parameters a λ_q a factor of around five wider than the ITPA-multi-machine scaling prediction [4]. The increase of λ_q reported here for the QCE regime is in a similar range with separatrix and scrape-off layer collisionality and density similar to the expected parameter for ITER. In the investigated ASDEX Upgrade discharges the origin of the filaments is identified to be close to the separatrix at the pedestal bottom [13]. So far, XCG1 simulations for medium-sized tokamaks with relative high collisionality at the pedestal top and the moderate temperature compared to ITER produced λ_q values not much above a poloidal gyro-radius scaling (see also [3]). However, a comparison of the reported experimental findings from ASDEX Upgrade to simulations of such conditions with XGC1 is of major interest for the challenge of power exhaust.

4. Origin of scrape-off layer broadening

To shed light on the origin of the λ_q broadening we investigate here the properties of the parallel and perpendicular heat transport in the scrape-off layer. Simultaneous measurements of divertor heat flux by IR thermography and electron kinetic profiles at the OMP by TS in attached L-mode and inter type-I ELM H-mode in ASDEX Upgrade demonstrated that the parallel heat transport is dominated by Spitzer–Härm electron heat conduction in these regimes [27,41]. In regimes with increased filamentary transport the importance of convection and ion heat conduction is increased [42]. To test whether not only changes in perpendicular transport but also in parallel transport are responsible for the broadening of the power fall-off length, we study target profiles and mid-plane profiles in more detail. Fig. 6 shows target heat flux from LPs (crosses with error bars) compared to the fitted profiles of the heat flux from IR (solid lines, profiles shown in the right figure of Fig. 2). The LP data is obtained by triple probes with a data acquisition at around 25 kHz, resolving single filaments in the QCE regime. The heat flux is calculated as shown in [43] assuming equal ion and electron temperature at the target. The LP heat flux is consistent with the IR based profiles, leading to the conclusion that the ratio of electron to ion heat transport at the divertor target does not significantly change with the disappearance of the type-I ELMs. However, no strike line sweep was performed leading to a poor spatial resolution of the LP data missing a crucial part around the heat flux peak from IR. Nevertheless, the broadening of the target heat flux profile is clearly observed also in the heat flux measured by LPs.

To further investigate the parallel heat transport we compare the temperature profile from TS and the corresponding electron temperature fall-off length with the power fall-off length from IR. The QCE regime is characterised by enhanced filament activity. Filaments in the scrape-off layer are linked to a so called density shoulder, in which the density in the far scrape-off layer has a flatter gradient than the near scrape-off layer decay [44].

Fig. 7 shows the electron kinetic profiles for # 36165 for the constant fuelling phase with no type-I ELMs between 5.0 s and 5.8 s in which the confinement time does not show a degradation. The grey dots represent the individual time points whereas the solid black line is a median filtered profile from 10 neighbouring radial positions. The horizontal black line in the left picture represents the separatrix electron temperature estimation using Spitzer–Härm electron heat conduction and two-thirds of P_{SOL} going to the outer target. The determination of the separatrix position can robustly be estimated if Spitzer–Härm electron heat conduction is dominant due to the strong temperature dependence [17,41,45]. The blue and red lines represent exponential fits performed in the corresponding intervals. The blue line represents the fit inside the separatrix, similar as done in [17]. In this region also a linear fit can be used [46]. In recent studies it was shown that the electron temperature gradient just inside the separatrix and in the near scrape-off layer are very similar in many regimes [17,32]. Due to the pedestal width varying only slightly, the similarity of the gradients just inside and just outside the separatrix is linked to a correlation between λ_q or λ_{T_e} in the near scrape-off layer with the pedestal top pressure as shown in [32,33]. Exceptions of the correlation between pedestal top pressure and near scrape-off layer fall-off length are reported when nitrogen seeding is used in ASDEX Upgrade [47]. As can be seen in Fig. 7 (left) the similarity between the pedestal gradient ($\lambda_{Te,in}$) and the scrape-off layer gradient ($\lambda_{Te,out}$) is broken for the QCE regime, which is beneficial for keeping the high confinement simultaneously with a broad scrape-off layer. This is not observed in studies using L, I and H-mode [30,32] or H-mode [33] where a broadening of the

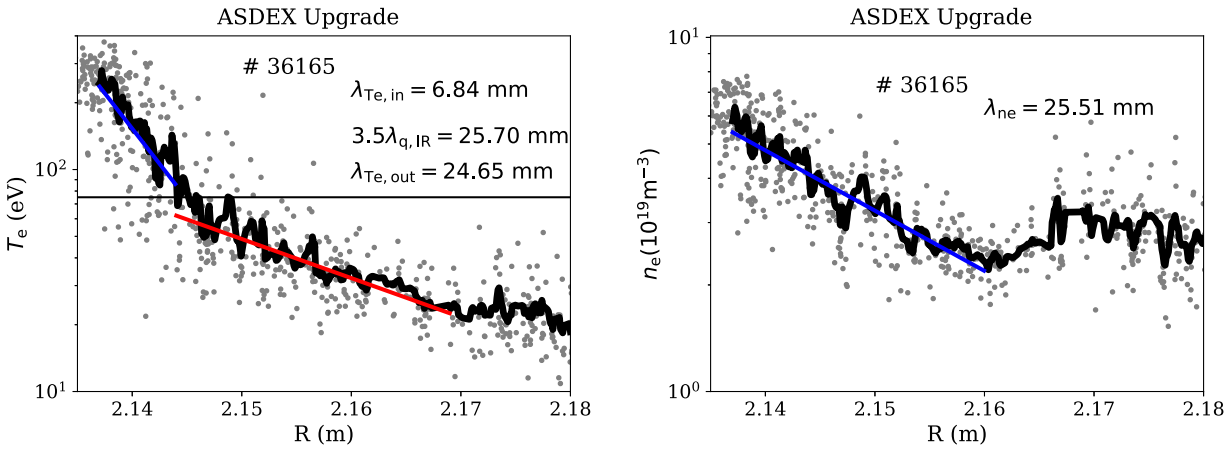

Fig. 7. Thomson scattering profiles for #36165 in the QCE regime of the electron temperate (left) and density (right). The grey dots show individual time points whereas the black lines represent a median filtered profile. The separatrix temperature is indicated with a horizontal line calculated from the IR power load. Exponential fits for inside (blue) and outside (red) data are shown for the temperature profile. The density profile is fitted with one exponential function up to 2.16 m (green).

scrape-off layer power fall-off length is linked to a loss of confinement by a reduction in pedestal top pressure. Furthermore, the near scrape-off layer λ_{T_e} and the λ_q are in line with Spitzer–Härm electron heat conduction. Interestingly, using the TS fitting as in [17] that leads to the scaling law as used in Eq. (3) the gradient length inside the separatrix is obtained. This might explain why the scaling law is not able to describe the broadening of power fall-off length λ_q since the link $\lambda_{Te,in} = \lambda_{Te,out} = 3.5 \cdot \lambda_q$ is broken in the QCE regime. Future studies are needed to investigate the conditions leading to the deviation between the two gradient lengths. In recent studies it was hypothesised that either the same mechanism (or co-dependence on e.g. B_{pol}) sets both gradient lengths or that the inside gradient is the drive for the outside gradient [32,33]. Following this argumentation, the QCE regime might have a second drive for the scrape-off layer that is not acting on the pedestal top. This second drive is in line with the idea that ballooning modes very close to the pedestal bottom lead to enhanced transport without degrading the pedestal top. The broader profile leads then to a reduction of separatrix electron temperature $T_{e,sep}$ from typically close to 100 eV for ASDEX Upgrade H-mode to around 75 eV assuming Spitzer–Härm electron heat conduction and two-thirds of P_{SOL} going to the outer target. This is consistent with using the parallel heat flux at the separatrix at the X-point deduced from the fit to the IR based heat flux profile. The lower temperature leads to a reduction of the Spitzer–Härm electron heat conduction increasing the effect of perpendicular transport further.

Fig. 7 (right) shows the density profile. The separatrix density is $n_{e,sep} \approx 4 \cdot 10^{19}\,m^{-3}$ or $n_{e,sep} \approx 0.4 \cdot n_{GW}$, close to a previously reported limit [9,10]. The density in the scrape-off layer flattens significantly to around $2 \cdot 10^{19}\,m^{-3}$, a clear sign of a density shoulder. A concern about the formation of the density shoulder are increased power loads on plasma facing components outside the divertor region. However, no significant temporal evolution of the power balance is observed, as discussed above. This hints towards first wall losses being small compared to the divertor power load in this discharge.

A more quantitative description of the perpendicular heat transport in the scrape-off layer, especially the interplay between steady state and filamentary transport was reported for L-mode [42]. Fig. 8 shows the temporal evolution of the power fall-off length λ_q, the turbulence parameter α_t and the filament frequency $f_{filament}$. All three are normalised to the respective values at 4.98 s ($f_{filament} = 2021$ Hz, $\lambda_q = 7.46$ mm and $\alpha_t = 0.47$). It is speculated that a higher value of α_t is linked to stronger turbulent activity as well as to a more ballooning unstable region inside the confined region close to the separatrix [17]. This region expels filaments into the scrape-off layer as can be seen by the increased detection rate of filaments in the far scrape-off layer measured by a thermal

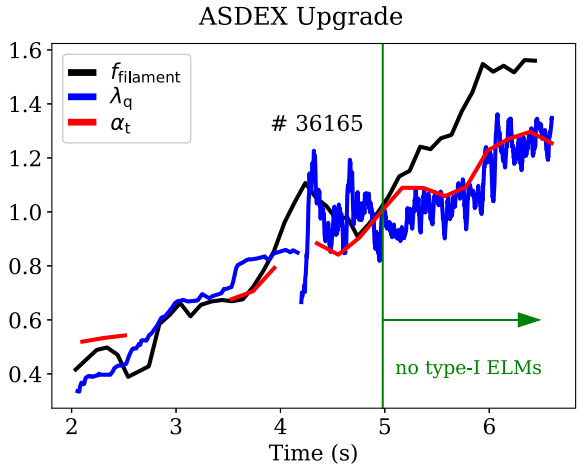

Fig. 8. Normalised filament frequency from THB (far SOL), turbulence parameter from TS (at separatrix, just inside) and power fall-off length (near SOL) from IR show all increase in similar way.

helium beam (THB) (see [25] for further details). Furthermore, close to the separatrix the THB measures broadband activity around 40 kHz also seen in ECE and Doppler reflectometry measurements in the confined region close to the separatrix that might be linked to such modes [8]. The radial convection of filaments was already investigated in the formation of the so called density shoulder at ASDEX Upgrade [44], a feature that is also present in this discharge and commonly observed in the QCE regime.

5. Discussion and conclusions

The absence of large scale transients due to the prevention of type-I ELMs without significant loss of confinement makes the QCE regime an attractive alternative reactor scenario. The operational space at high separatrix density and high shaping will be relevant also for next step devices like ITER.

We have shown that the power fall-off length increases up to a factor of four compared to the inter type-I ELM H-mode regime used for the ITPA-multi-machine scaling law. Such a broadening without degraded confinement is so far uniquely observed in the QCE regime. The broadened scrape-off layer not only reduces the peak power load in attached conditions. Together with high separatrix density models [12,48,49]

indicate that detachment can be reached already at reduced impurity concentrations.

The parallel heat transport in the QCE regime is in line with Spitzer–Härm electron heat conduction. The broadening of λ_q is linked to an increased filament frequency and radial propagation velocity, as well as a higher pressure close to the separatrix. Our hypothesis is that the higher pressure leads to ballooning modes being more unstable expelling more filaments into the scrape-off layer. The filaments transport particles and heat further into the scrape-off layer where they cool through Spitzer–Härm electron heat conduction. Future work will analyse the parallel transport on a time scale faster than of the filaments using e.g. the THB. This will allow to address the fluctuation amplitude as well as the non-linear processes between temperature and heat flux. The formation of a density shoulder in the QCE regime gives further evidence of the enhanced perpendicular transport.

An open point for power exhaust in the QCE regime is the integration of a detached divertor. Although the filaments appear as a quasi-continuous flux towards the divertor, single filaments lead locally to enhanced temperature and particle flux. The interaction between the filaments and detachment induced by impurity seeding is focus of future studies.

Regarding the extrapolation of the QCE regime to future larger devices we can consider the following: (i) the collisionality at the separatrix is very similar and so is the turbulence parameter α_T. (ii) The instability of ballooning modes can be analysed only with non-linear resistive modelling. (iii) The size of filaments can result from such modelling efforts. Only if all these ingredients are available it can be estimated whether the larger divertor volume with its increased buffering capability can tolerate the filamentary heat flux.

Declaration of competing interest

The authors declare that they have no known competing financial interests or personal relationships that could have appeared to influence the work reported in this paper.

Acknowledgement

This work has been carried out within the framework of the EUROfusion Consortium and has received funding from the Euratom research and training programme 2014–2018 and 2019–2020 under grant agreement No 633053. The views and opinions expressed herein do not necessarily reflect those of the European Commission. G.F. Harrer is a Fellow of the Friedrich Schiedel Foundation for Energy Technology.

References

[1] T. Eich, B. Sieglin, A. Scarabosio, W. Fundamenski, R.J. Goldston, A. Herrmann, [ASDEX Upgrade Team Collaboration], Phys. Rev. Lett. 107 (2011) 215001.

[2] T. Eich, A.W. Leonard, R.A. Pitts, W. Fundamenski, R.J. Goldston, T.K. Gray, A. Herrmann, A. Kirk, A. Kallenbach, O. Kardaun, A.S. Kukushkin, B. LaBombard, R. Maingi, M.A. Makowski, A. Scarabosio, B. Sieglin, J. Terry, A. Thornton, ASDEX Upgrade Team, JET EFDA Contributors, Nucl. Fusion 53 (9) (2013) 093031.

[3] R.J. Goldston, Nucl. Fusion 52 (1) (2012) 013009.

[4] C.S. Chang, S. Ku, A. Loarte, V. Parail, F. Köchl, M. Romanelli, R. Maingi, J.-W. Ahn, T. Gray, J. Hughes, B. LaBombard, T. Leonard, M. Makowski, J. Terry, Nucl. Fusion 57 (11) (2017) 116023.

[5] A. Loarte, G. Huijsmans, S. Futatani, L.R. Baylor, T.E. Evans, D.M. Orlov, O. Schmitz, M. Becoulet, P. Cahyna, Y. Gribov, A. Kavin, A. Sashala Naik, D.J. Campbell, T. Casper, E. Daly, H. Frerichs, A. Kischner, R. Laengner, S. Lisgo, R.A. Pitts, G. Saibene, A. Wingen, Nucl. Fusion 54 (3) (2014) 033007.

[6] G. Federici, C. Bachmann, L. Barucca, C. Baylard, W. Biel, L.V. Boccaccini, C. Bustreo, S. Ciattaglia, F. Cismondi, V. Corato, C. Day, E. Diegele, T. Franke, E. Gaio, C. Gliss, T. Haertl, A. Ibarra, J. Holden, G. Keech, R. Kembleton, A. Loving, F. Maviglia, J. Morris, B. Meszaros, I. Moscato, G. Pintsuk, M. Siccinio, N. Taylor, M.Q. Tran, C. Vorpahl, H. Walden, J.H. You, Nucl. Fusion 59 (6) (2019) 066013.

[7] J. Stober, M. Maraschek, G.D. Conway, O. Gruber, A. Herrmann, A.C.C. Sips, W. Treutterer, H. Zohm, ASDEX Upgrade Team, Nucl. Fusion 41 (9) (2001) 1123–1134.

[8] E. Wolfrum, M. Bernert, J.E. Boom, A. Burckhart, I.G.J. Classen, G.D. Conway, T. Eich, R. Fischer, A. Gude, A. Herrmann, N.C. Luhmann, M. Maraschek, R. McDermott, H.K. Park, T. Pütterich, J. Vicente, B. Wieland, M. Willensdorfer, the ASDEX Upgrade Team, Plasma Phys. Control. Fusion 53 (8) (2011) 085026.

[9] M. Bernert, T. Eich, A. Kallenbach, D. Carralero, A. Huber, P.T. Lang, S. Potzel, F. Reimold, J. Schweinzer, E. Viezzer, H. Zohm, Plasma Phys. Control. Fusion 57 (1) (2014) 014038.

[10] T. Eich, R.J. Goldston, A. Kallenbach, B. Sieglin, H.J. Sun, ASDEX Upgrade Team, JET Contributors, Nucl. Fusion 58 (3) (2018) 034001.

[11] A.S. Kukushkin, H.D. Pacher, G.W. Pacher, V. Kotov, R.A. Pitts, D. Reiter, Journal of Nuclear Materials 438 (2013) S203–S207, Proceedings of the 20th International Conference on Plasma-Surface Interactions in Controlled Fusion Devices.

[12] R.J. Goldston, M.L. Reinke, J.A. Schwartz, Plasma Phys. Control. Fusion 59 (5) (2017) 055015.

[13] G.F. Harrer, E. Wolfrum, M.G. Dunne, P. Manz, M. Cavedon, P.T. Lang, B. Kurzan, T. Eich, B. Labit, J. Stober, H. Meyer, M. Bernert, F.M. Laggner, F. Aumayr, the EUROfusion MST1 Team, the ASDEX Upgrade Team, Nucl. Fusion 58 (11) (2018) 112001.

[14] B. Labit, T. Eich, G.F. Harrer, E. Wolfrum, M. Bernert, M.G. Dunne, L. Frassinetti, P. Hennequin, R. Maurizio, A. Merle, H. Meyer, S. Saarelma, U. Sheikh, J. Adamek, M. Agostini, D. Aguiam, R. Akers, R. Albanese, C. Albert, E. Alessi, R. Ambrosino, Y. Andrèbe, C. Angioni, G. Apruzzese, M. Aradi, H. Arnichand, F. Auriemma, G. Avdeeva, J.M. Ayllon-Guerola, F. Bagnato, V.K. Bandaru, M. Barnes, L. Barrera-Orte, P. Bettini, R. Bilato, O. Biletskyi, P. Bilkova, W. Bin, P. Blanchard, T. Blanken, V. Bobkov, A. Bock, D. Boeyaert, K. Bogar, O. Bogar, P. Bohm, T. Bolzonella, F. Bombarda, L. Boncagni, F. Bouquey, C. Bowman, S. Brezinsek, D. Brida, D. Brunetti, J. Bucalossi, J. Buchanan, J. Buermans, H. Bufferand, S. Buller, P. Buratti, A. Burckhart, G. Calabrò, L. Calacci, Y. Camenen, B. Cannas, P. Cano Megías, D. Carnevale, F. Carpanese, M. Carr, D. Carralero, L. Carraro, A. Casolari, A. Cathey, F. Causa, M. Cavedon, M. Cecconello, S. Ceccuzzi, J. Cerovsky, S. Chapman, P. Chmielewski, D. Choi, C. Cianfarani, G. Ciraolo, S. Coda, R. Coelho, L. Colas, D. Colette, L. Cordaro, F. Cordella, S. Costea, D. Coster, D.J. Cruz Zabala, G. Cseh, A. Czarnecka, I. Cziegler, O. D'Arcangelo, A. Dal Molin, P. David, G. De Carolis, H. De Oliveira, J. Decker, R. Dejarnac, R. Delogu, N. den Harder, M. Dimitrova, F. Dolizy, J.J. Domínguez-Palacios Durán, D. Douai, A. Drenik, M. Dreval, B. Dudson, D. Dunai, B.P. Duval, R. Dux, S. Elmore, O. Embréus, B. Erdõs, E. Fable, M. Faitsch, A. Fanni, M. Farnik, I. Faust, J. Faustin, N. Fedorczak, F. Felici, S. Feng, X. Feng, J. Ferreira, G. Ferrò, O. Février, O. Ficker, L. Figini, A. Figueiredo, A. Fil, M. Fontana, M. Francesco, C. Fuchs, S. Futatani, L. Gabellieri, D. Gadariya, D. Gahle, D. Galassi, K. Galazka, J. Galdon-Quiroga, S. Galeani, D. Gallart, A. Gallo, C. Galperti, S. Garavaglia, J. Garcia, J. Garcia-Lopez, M. Garcia-Muñoz, L. Garzotti, J. Gath, B. Geiger, L. Giacomelli, L. Giannone, S. Gibson, L. Gil, E. Giovannozzi, G. Giruzzi, M. Gobbin, J. Gonzalez-Martin, T.P. Goodman, G. Gorini, M. Gospodarczyk, G. Granucci, D. Grekov, G. Grenfell, M. Griener, M. Groth, O. Grover, M. Gruca, A. Gude, L. Guimarais, T. Gyergyek, P. Hacek, A. Hakola, C. Ham, T. Happel, J. Harrison, A. Havranek, J. Hawke, S. Henderson, L. Hesslow, F. Hitzler, B. Hnat, J. Hobirk, M. Hölzl, D. Hogeweij, C. Hopf, M. Hoppe, J. Horacek, M. Hron, Z. Huang, A. Iantchenko, D. Iglesias, V. Igochine, P. Innocente, C. Ionita-Schrittwieser, H. Isliker, I. Ivanova-Stanik, A. Jacobsen, M. Jakubowski, F. Janky, A. Jardin, F. Jaulmes, T. Jensen, T. Jonsson, A. Kallenbach, A. Kappatou, A. Karpushov, S. Kasilov, Y. Kazakov, P.V. Kazantzidis, D. Keeling, M. Kelemen, A. Kendl, W. Kernbichler, A. Kirk, G. Kocsis, M. Komm, M. Kong, V. Korovin, M. Koubiti, J. Kovacic, N. Krawczyk, K. Krieger, L. Kripner, A. Křivská, O. Kudlacek, Y. Kulyk, T. Kurki-Suonio, R. Kwiatkowski, F. Laggner, L. Laguardia, A. Lahtinen, P. Lang, J. Likonen, B. Lipschultz, F. Liu, R. Lombroni, R. Lorenzini, V.P. Loschiavo, T. Lunt, E. Macusova, J. Madsen, R. Maggiora, B. Maljaars, P. Manas, P. Mantica, M.J. Mantsinen, P. Manz, M. Maraschek, V. Marchenko, C. Marchetto, A. Mariani, C. Marini, T. Markovic, L. Marrelli, P. Martin, J.R. Martín Solís, A. Martitsch, S. Mastrostefano, F. Matos, G. Matthews, M.-L. Mayoral, D. Mazon, C. Mazzotta, P. Mc Carthy, K. McClements, R. McDermott, B. Mcmillan, C. Meineri, V. Menkovski, D. Meshcheriakov, M. Messmer, D. Micheletti, D. Milanesio, F. Militello, I.G. Miron, J. Mlynar, V. Moiseenko, P.A. Molina Cabrera, J. Morales, J.-M. Moret, A. Moro, D. Moulton, F. Nabais, V. Naulin, D. Naydenkova, R.D. Nem, F. Nespoli, S. Newton, A.H. Nielsen, S.K. Nielsen, V. Nikolaeva, M. Nocente, S. Nowak, M. Oberkofler, R. Ochoukov, P. Ollus, J. Olsen, J. Omotani, J. Ongena, F. Orain, F.P. Orsitto, R. Paccagnella, A. Palha, L. Panaccione, R. Panek, M. Panjan, G. Papp, I. Paradela Perez, F. Parra, M. Passeri, A. Pau, G. Pautasso, R. Pavlichenko, A. Perek, V. Pericoli Radolfini, F. Pesamosca, M. Peterka, V. Petrzilka, V. Piergotti, L. Pigatto, P. Piovesan, C. Piron, L. Piron, V. Plyusnin, G. Pokol, E. Poli, P. Pölöskei, T. Popov, Z. Popovic, G. Pór, L. Porte, G. Pucella, M.E. Puiatti, T. Pütterich, M. Rabinski, J. Juul Rasmussen, J. Rasmussen, G.A. Rattá, S. Ratynskaia, T. Ravensbergen, D. Réfy, M. Reich, H. Reimerdes, F. Reimold, D. Reiser, C. Reux, S. Reznik, D. Ricci, N. Rispoli, J.F. Rivero-Rodriguez, G. Rocchi, M. Rodriguez-Ramos, A. Romano, J. Rosato, G. Rubinacci, G. Rubino, D.A. Ryan, M. Salewski, A. Salmi, D. Samaddar, L. Sanchis-Sanchez, J. Santos, K. Särkimäki, M. Sassano, O. Sauter, R. Scannell, M. Scheffer, B.S. Schneider, P. Schneider, R. Schrittwieser, M. Schubert, J. Seidl, E. Seliunin, S. Sharapov, R.R. Sheeba, G. Sias, B. Sieglin, C. Silva, S. Sipilä, S. Smith, A. Snicker, E.R. Solano, S.K. Hansen, C. Soria-Hoyo, E.

Sorokovoy, C. Sozzi, A. Sperduti, G. Spizzo, M. Spolaore, M. Stejner, L. Stipani, J. Stober, P. Strand, H. Sun, W. Suttrop, D. Sytnykov, T. Szepesi, B. Tál, T. Tala, G. Tardini, M. Tardocchi, A. Teplukhina, D. Terranova, D. Testa, C. Theiler, E. Thorén, A. Thornton, B. Tilia, P. Tolias, M. Tomes, M. Toscano-Jimenez, C. Tsironis, C. Tsui, O. Tudisco, J. Urban, M. Valisa, M. Vallar, P. Vallejos Olivares, M. Valovic, D. Van Vugt, B. Vanovac, J. Varje, J. Varju, S. Varoutis, S. Vartanian, O. Vasilovici, J. Vega, G. Verdoolaege, K. Verhaegh, L. Vermare, N. Vianello, J. Vicente, E. Viezzer, F. Villone, I. Voitsekhovitch, D. Voltolina, P. Vondracek, N.M.T. Vu, N. Walkden, T. Wauters, M. Weiland, V. Weinzettl, M. Wensing, S. Wiesen, M. Wiesenberger, G. Wilkie, M. Willensdorfer, M. Wischmeier, K. Wu, L. Xiang, R. Zagorski, D. Zaloga, P. Zanca, R. Zaplotnik, J. Zebrowski, W. Zhang, A. Zisis, S. Zoletnik, M. Zuin, Nucl. Fusion 59 (8) (2019) 086020.

[15] G. Saibene, P.J. Lomas, R. Sartori, A. Loarte, J. Stober, Y. Andrew, S.A. Arshad, G.D. Conway, E. de la Luna, K. Günther, L.C. Ingesson, M.A.H. Kempenaars, A. Korotkov, H.R. Koslowski, J.S. Lönnroth, D.C. McDonald, A. Meigs, P. Monier-Garbet, V. Parail, C.P. Perez, F.G. Rimini, S. Sharapov, P.R. Thomas, Nucl. Fusion 45 (5) (2005) 297–317.

[16] A. Kirk, H.W. Muller, E. Wolfrum, H. Meyer, A. Herrmann, T. Lunt, V. Rohde, P. Tamain, the MAST and ASDEX Upgrade Team, Plasma Phys. Control. Fusion 53 (9) (2011) 095008.

[17] T. Eich, P. Manz, R.J. Goldston, P. Hennequin, P. David, M. Faitsch, B. Kurzan, B. Sieglin, E. Wolfrum, the ASDEX Upgrade Team, the EUROfusion MST1 Team, Nucl. Fusion 60 (5) (2020) 056016.

[18] A. Mlynek, G. Schramm, H. Eixenberger, G. Sips, K. McCormick, M. Zilker, K. Behler, J. Eheberg, ASDEX Upgrade Team, Rev. Sci. Instrum. 81 (3) (2010) 033507.

[19] A. Kallenbach, R. Dux, J.C. Fuchs, R. Fischer, B. Geiger, L. Giannone, A. Herrmann, T. Lunt, V. Mertens, R. McDermott, R. Neu, T. Pütterich, S. Rathgeber, V. Rohde, K. Schmid, J. Schweinzer, W. Treutterer, the ASDEX Upgrade Team, Plasma Phys. Control. Fusion 52 (5) (2010) 055002.

[20] A. Kallenbach, M. Bernert, M. Beurskens, L. Casali, M. Dunne, T. Eich, L. Giannone, A. Herrmann, M. Maraschek, S. Potzel, F. Reimold, V. Rohde, J. Schweinzer, E. Viezzer, M. Wischmeier, the ASDEX Upgrade Team, Nucl. Fusion 55 (5) (2015) 053026.

[21] B. Sieglin, M. Faitsch, A. Herrmann, B. Brucker, T. Eich, L. Kammerloher, S. Martinov, Rev. Sci. Instrum. 86 (11) (2015) 113502.

[22] D. Nille, U. von Toussaint, B. Sieglin, M. Faitsch, Bayesian Inference and Maximum Entropy Methods in Science and Engineering, Springer International Publishing, Cham, 2018, pp. 55–64.

[23] A. Herrmann, W. Junker, K. Guenther, S. Bosch, M. Kaufmann, J. Neuhauser, G. Pautasso, Th Richter, R. Schneider, Plasma Phys. Control. Fusion 37 (1) (1995) 17.

[24] A. Herrmann, ASDEX Upgrade Team, Proc. 28th EPS Conf. on Controlled Fusion and Plasma Physics, Madeira, Portugal, 2001) ECA Vol 25A P 2109, CD-ROM, 2001, p. 2109.

[25] M. Griener, E. Wolfrum, G. Birkenmeier, M. Faitsch, R. Fischer, G. Fuchert, L. Gil, G.F. Harrer, P. Manz, D. Wendler, U. Stroth, the ASDEX Upgrade Team, the EUROfusion MST1 Team, Nuclear Materials and Energy (2020) 100854.

[26] P. David, M. Bernert, T. Puetterich, J.C. Fuchs, S. Gloeggler, T. Eich, the ASDEX Upgrade Team, Nucl. Fusion (2020) in preparation.

[27] M. Faitsch, B. Sieglin, T. Eich, H.J. Sun, A. Herrmann, the ASDEX Upgrade Team, Plasma Phys. Control. Fusion 57 (7) (2015) 075005.

[28] M. Bernert, M. Wischmeier, A. Huber, F. Reimold, B. Lipschultz, C. Lowry, S. Brezinsek, R. Dux, T. Eich, A. Kallenbach, A. Lebschy, C. Maggi, R. McDermott, T. Pütterich, S. Wiesen, Nuclear Mater. Energy 12 (2017) 111–118.

[29] M. Griener, E. Wolfrum, M. Cavedon, R. Dux, V. Rohde, M. Sochor, J.M. Munoz Burgos, O. Schmitz, U. Stroth, Rev. Sci. Instrum. 89 (10) (2018) 10D102.

[30] D. Brunner, B. LaBombard, A.Q. Kuang, J.L. Terry, Nucl. Fusion 58 (9) (2018) 094002.

[31] M. Faitsch, R. Maurizio, A. Gallo, S. Coda, T. Eich, B. Labit, A. Merle, H. Reimerdes, B. Sieglin, C. Theiler, the Eurofusion MST1 Team, the TCV Team, Plasma Phys. Control. Fusion 60 (4) (2018) 045010.

[32] D. Silvagni, T. Eich, M. Faitsch, T. Happel, B. Sieglin, P. David, D. Nille, L. Gil, U. Stroth, the EUROfusion MST1 Team, the ASDEX Upgrade Team, Plasma Phys. Control. Fusion 62 (4) (2020) 045015.

[33] M. Faitsch, T. Eich, B. Sieglin, JET contributors, Plasma Phys. Control. Fusion 62 (8) (2020) 085004.

[34] ITER Physics Expert Group on Confinement and Transport, ITER Physics Expert Group on Confinement Modelling and Database, ITER Physics Basis Editors, Nucl. Fusion 39 (12) (1999) 2175.

[35] R. Fischer, C.J. Fuchs, B. Kurzan, W. Suttrop, E. Wolfrum, Fusion Sci. Technol. 58 (2) (2010) 675–684.

[36] O.J.W.F. KARDAUN, et al., Proc. 21st IAEA Fusion Energy Conference, Chengdu, PRC, IAEA, 2006.

[37] G. Verdoolaege, S. M Kaye, C. Angioni, O. JWF Kardaun, M. Maslov, M. Romanelli, F. Ryter, K. Thomsen, Nucl. Fusion (2020) in preparation.

[38] P.T. Lang, C. Angioni, M. Bernert, A. Bock, T.M.J. Engelhardt, R. Fischer, O.J.W.F. Kardaun, B. Ploeckl, M. Prechtl, W. Suttrop, G. Tardini, M. Wischmeier, E. Wolfrum, H. Zohm, the ASDEX Upgrade Team, Nucl. Fusion 60 (9) (2020) 092003.

[39] Martin Greenwald, Plasma Phys. Control. Fusion 44 (8) (2002) R27.

[40] B. Kurzan, H.D. Murmann, Rev. Sci. Instrum. 82 (10) (2011) 103501.

[41] H.J. Sun, E. Wolfrum, T. Eich, B. Kurzan, S. Potzel, U. Stroth, the ASDEX Upgrade Team, Plasma Phys. Control. Fusion 57 (12) (2015) 125011.

[42] D. Carralero, S. Artene, M. Bernert, G. Birkenmeier, M. Faitsch, P. Manz, P. de Marne, U. Stroth, M. Wischmeier, E. Wolfrum, The ASDEX Upgrade Team, The EURO-fusion MST1 Team, Nucl. Fusion 58 (9) (2018) 096015.

[43] D. Brida, T. Lunt, M. Wischmeier, M. Bernert, D. Carralero, M. Faitsch, Y. Feng, T. Sehmer, B. Sieglin, W. Suttrop, E. Wolfrum, the ASDEX Upgrade Team, the MST1 Team, Nucl. Fusion 57 (11) (2017) 116006.

[44] D. Carralero, G. Birkenmeier, H.W. Müller, P. Manz, P. deMarne, S.H. Müller, F. Reimold, U. Stroth, M. Wischmeier, E. Wolfrum, The ASDEX Upgrade Team, Nucl. Fusion 54 (12) (2014) 123005.

[45] M. Faitsch, B. Sieglin, T. Eich, A. Herrmann, W. Suttrop, the ASDEX Upgrade Team, Plasma Phys. Control. Fusion 59 (9) (2017) 095006.

[46] P.A. Schneider, E. Wolfrum, R.J. Groebner, T.H. Osborne, M.N.A. Beurskens, M.G. Dunne, J.R. Ferron, S. Günter, B. Kurzan, K. Lackner, P.B. Snyder, H. Zohm, the ASDEX Upgrade Team, the DIII-D Team, JET EFDA Contributors, Plasma Phys. Control. Fusion 54 (10) (2012) 105009.

[47] H.J. Sun, E. Wolfrum, T. Eich, A. Kallenbach, P. Schneider, B. Kurzan, U. Stroth, the ASDEX Upgrade Team, Plasma Phys. Control. Fusion 62 (2) (2019) 025005.

[48] M.L. Reinke, Nucl. Fusion 57 (3) (2017) 034004.

[49] A. Kallenbach, H.J. Sun, T. Eich, D. Carralero, J. Hobirk, A. Scarabosio, M. Siccinio, the ASDEX Upgrade Team, the EUROfusion MST1 Team, Plasma Phys. Control. Fusion 60 (4) (2018) 045006.